Available online at www.sciencedirect.com
SCIENCE DIRECT®
Tetrahedron Letters 46 (2005) 7631–7635
Tetrahedron Letters

Spectroscopic and DFT studies of nonclassical and classical radical cations of 7-benzhydrylidenenorbornene analogues: contrasting molecular geometry and electronic structures originating from the different patterns of electronic coupling

Hiroshi Ikeda,[a,*] Hayato Namai[a] and Takashi Hirano[b]

[a]*Department of Chemistry, Graduate School of Science, Tohoku University, Sendai 980-8578, Japan*
[b]*Department of Applied Physics and Chemistry, The University of Electro-Communications, Chofu, Tokyo 182-8585, Japan*

Received 13 July 2005; revised 10 August 2005; accepted 19 August 2005

Abstract—Nanosecond time-resolved UV/vis absorption spectroscopy on laser flash photolysis and calculations based on (time-dependent) density functional theory for radical cations of 7-benzhydrylidenebenzonorbornene (**3**) and 7-benzhydrylidene-2,3-dimethylenenorbornane (**4**) indicated their contrasting molecular geometry and electronic structures, suggesting the nonclassical and classical nature of $\mathbf{3}^{\bullet+}$ and $\mathbf{4}^{\bullet+}$, respectively, which originated from the different patterns of electronic coupling between the C-7–C-8 and C-2–C-3 subunits.

Recently, we studied[1] nanosecond time-resolved UV/vis absorption spectroscopy on laser flash photolysis (LFP) under photoinduced electron-transfer (PET) conditions and density functional theory (DFT) calculations for radical cations of 7-benzhydrylidenenorbornane (**1**, Chart 1) and 7-benzhydrylidenenorbornene (**2**), and provided evidence for the nonclassical nature of $\mathbf{2}^{\bullet+}$.[2,4] Owing to electronic coupling, recognized as a homoconjugation,[6] between the C-7–C-8 and C-2–C-3 subunits, $\mathbf{2}^{\bullet+}$ possesses a bent structure, in which spin and charge are considerably delocalized, not only to the benzhydrylidene subunit but also to the residual subunit

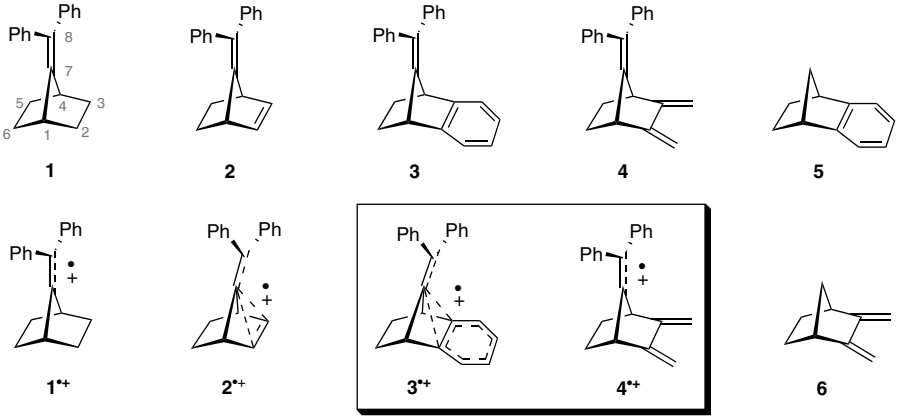

Chart 1. A list of 7-benzhydrylidenenorbornane derivatives (**1**–**4**), the corresponding radical cations ($\mathbf{1}^{\bullet+}$–$\mathbf{4}^{\bullet+}$), and related compounds (**5** and **6**).

Keywords: Photochemistry; Nonclassical radical cation; DFT calculation; Absorption spectra; Electronic coupling; Molecular geometry.
* Corresponding author. Fax (internat.): +81 22 795 6557; e-mail: ikeda@org.chem.tohoku.ac.jp

0040-4039/$ - see front matter © 2005 Elsevier Ltd. All rights reserved.
doi:10.1016/j.tetlet.2005.08.167

(vide infra). In other words, the p-orbitals at C-2 and C-3 hold the key to producing radical cations with the non-classical nature in the 7-benzhydrylidenenorbornene system. From this perspective, it is of interest to examine the nature of radical cations of the structurally related 7-benzhydrylidenebenzonorbornene (**3**)[7] and 7-benzhydrylidene-2,3-dimethylenenorbornane (**4**),[7] which have p-orbitals at the C-2 and C-3 sites. While the previous exploratory study[7] implied some difference in electronic coupling of $\mathbf{3}^{\bullet+}$ and $\mathbf{4}^{\bullet+}$, detailed investigation of them using spectroscopy and the latest theoretical calculation was not available yet. Therefore, we conducted, in this work, nanosecond time-resolved UV/vis absorption spectroscopy on LFP under PET conditions, together with DFT and time-dependent (TD) DFT calculations for them. Here, we report the striking contrast in the molecular geometry and electronic structures of $\mathbf{3}^{\bullet+}$ and $\mathbf{4}^{\bullet+}$.

Nanosecond time-resolved UV/vis absorption spectroscopy on LFP[9] was performed with *N*-methylquinolinium tetrafluoroborate ($NMQ^+BF_4^-$) and toluene as the sensitizer and cosensitizer,[10] respectively, in aerated acetonitrile at 298 K. As Figure 1 shows, laser excitation (355 nm) of $NMQ^+BF_4^-$ with **3** and **4** in aerated acetonitrile gave the characteristic absorption bands of $\mathbf{3}^{\bullet+}$ and $\mathbf{4}^{\bullet+}$, respectively. Radical cation $\mathbf{3}^{\bullet+}$ exhibited an intense, sharp absorption band with λ_{ab} at 401 nm (band A′), a broad, weak absorption band at 480–580 nm (band B′), and a broad, intense absorption band at >600 nm (band C′) [Fig. 1 (red)].[11] Similarly, $\mathbf{4}^{\bullet+}$ had an intense, sharp absorption band with λ_{ab} at 394 nm (band A″), a broad, weak absorption band at 500–650 nm (band B″), and a broad, intense absorption band at >700 nm (band C″) [Fig. 1 (green)].[11]

The absorption bands of $\mathbf{3}^{\bullet+}$ and $\mathbf{4}^{\bullet+}$ were compared with those of $\mathbf{1}^{\bullet+}$: an intense, sharp absorption band with λ_{ab} at 386 nm (band A), a broad, weak absorption band at 500–650 nm (band B), and a broad, intense absorption band at >700 nm (band C).[1] Band A′ (401 nm) of $\mathbf{3}^{\bullet+}$ was redshifted as compared with band A (386 nm) of $\mathbf{1}^{\bullet+}$, while blueshifts were observed for band B′ (480–580 nm) and band C′ (>600 nm) of $\mathbf{3}^{\bullet+}$ as compared with bands B and C (500–650 and >700 nm, respectively) of $\mathbf{1}^{\bullet+}$. Interestingly, band A″ (394 nm) of $\mathbf{4}^{\bullet+}$ was redshifted slightly as compared with band A (386 nm) of $\mathbf{1}^{\bullet+}$, while no shifts were observed for bands B″ and C″ (500–650 and >700 nm, respectively) of $\mathbf{4}^{\bullet+}$ as compared with bands B and C of $\mathbf{1}^{\bullet+}$, respectively.

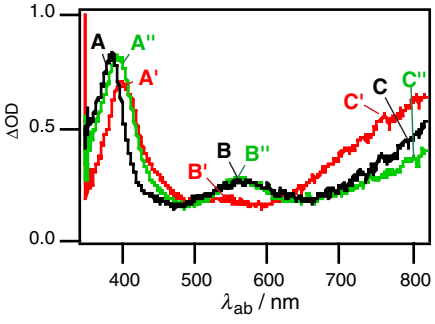

Figure 1. Nanosecond time-resolved UV/vis absorption spectra observed 100 ns after the laser pulse on LFP of **1** (black, 1 mM), **3** (red, 1 mM), and **4** (green, 1 mM), under $NMQ^+BF_4^-$ (10 mM)–toluene (1 M)-sensitized conditions in aerated acetonitrile.

To evaluate the spectroscopic properties as well as to gain insight into the molecular geometry and electronic structures of $\mathbf{3}^{\bullet+}$ and $\mathbf{4}^{\bullet+}$, we performed DFT and TD DFT calculations[12] for **3**, **4**, and the corresponding radical cations, and compared the results with those of **1**, **2**, and the corresponding radical cations. The electronic transition wavelengths (λ_{et}) and oscillator strengths (f) of $\mathbf{3}^{\bullet+}$ and $\mathbf{4}^{\bullet+}$ in the optimized structures (vide infra) were calculated using TD UB3LYP/cc-pVDZ and are shown in Figure 2 together with those of $\mathbf{1}^{\bullet+}$.[1] The calculations gave λ_{et} at 353, 554, and 780 nm with $f = 0.153$, 0.027, and 0.094 for $\mathbf{1}^{\bullet+}$,[1] λ_{et} at 371, 517, and 745 nm with $f = 0.140$, 0.014, and 0.074 for $\mathbf{3}^{\bullet+}$ and λ_{et} at 360, 557, and 779 nm with $f = 0.196$, 0.042, and 0.089 for $\mathbf{4}^{\bullet+}$, respectively. These calculated electronic transitions successfully reproduced the observed red- and blueshifts of λ_{ab} of $\mathbf{3}^{\bullet+}$ and $\mathbf{4}^{\bullet+}$ as compared with those of $\mathbf{1}^{\bullet+}$ (Fig. 1).

Figure 3 shows the concept of the electronic coupling in neutral substrates **3** and **4** graphically. Note that the molecular orbitals (MOs) of **3** are derived from those of the ethylene and benzo subunits of **1** and benzonorbornene (**5**, Chart 1), respectively, while the MOs of the ethylene and 1,3-butadiene subunits of **1** and 2,3-dimethylenenorbornane (**6**), respectively, represent those of **4**. A combination of the highest occupied MOs (HOMOs) of **1** and **5** allows them to interact with each other efficiently to give the HOMO of **3** with an antibonding character, because the three orbitals at C-7 of

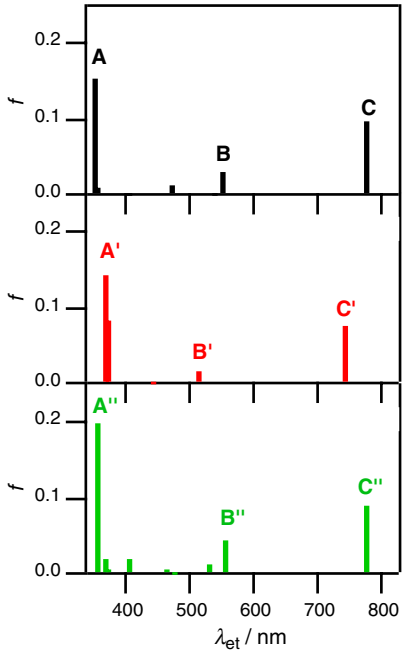

Figure 2. Electronic transitions of $\mathbf{1}^{\bullet+}$ (black), $\mathbf{3}^{\bullet+}$ (red), and $\mathbf{4}^{\bullet+}$ (green) calculated using TD UB3LYP/cc-pVDZ.

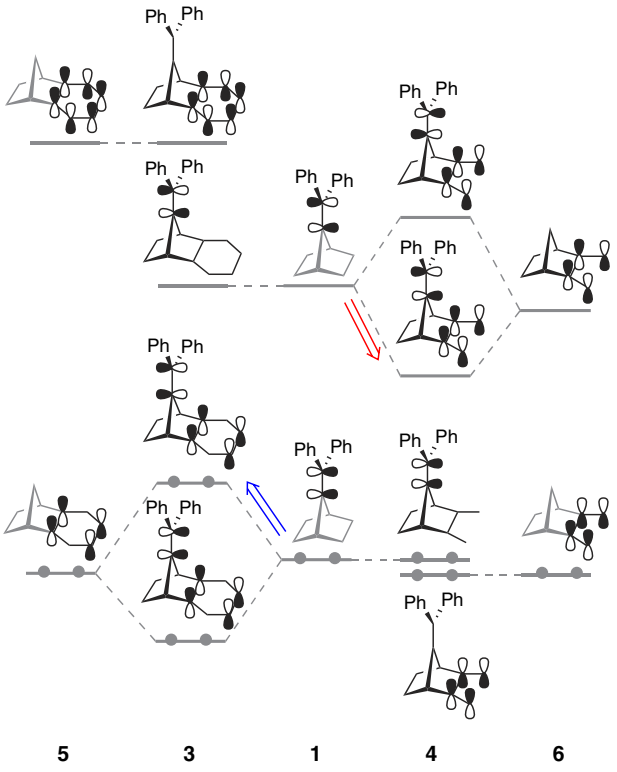

Figure 3. Conceptual representation showing the electronic coupling of **1** with **5** and **6** to give **3** and **4**, respectively. Red and blue thick arrows indicate the lowering of the LUMO level of **4** and the rise in the HOMO level of **3**, respectively, as compared with **1**.

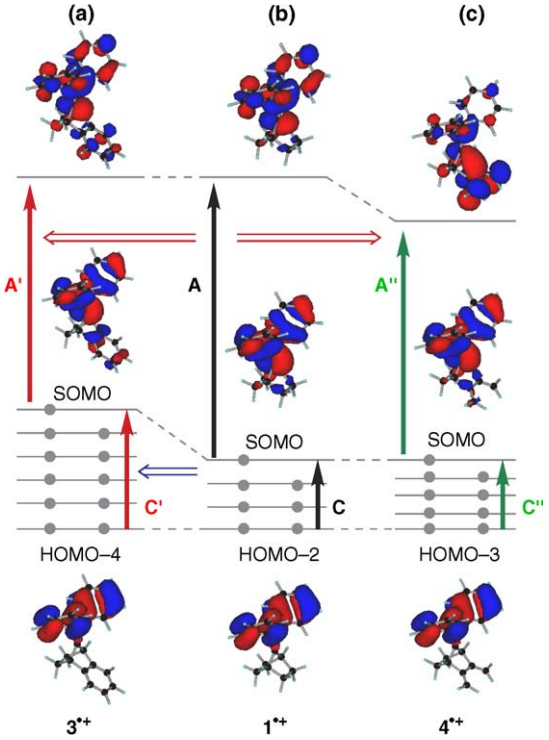

Figure 4. Schematic representation of the MOs of $\mathbf{3}^{\bullet+}$ (a), $\mathbf{1}^{\bullet+}$ (b), and $\mathbf{4}^{\bullet+}$ (c) associated with bands A, A′, and A″ and C, C′, and C″. Thick red arrows indicate the redshifts of band A′ for $\mathbf{3}^{\bullet+}$ and band A″ for $\mathbf{4}^{\bullet+}$ as compared with $\mathbf{1}^{\bullet+}$, while the blueshift of band C′ for $\mathbf{3}^{\bullet+}$ is shown with a thick blue arrow.

1 and at C-2 and C-3 of **5** are in phase with each other. A similar electronic coupling between the lowest unoccupied MOs (LUMOs) of **1** and **5** is possible in terms of the topological agreement of the orbitals at C-7 of **1** and at C-2 and C-3 of **5**, but is prevented by the large energy gap (0.66 eV with B3LYP/cc-pVDZ calculation) between them. Interestingly, similar electronic coupling in the HOMOs of **1** and **6** is cancelled by the topological disagreement of the orbitals at C-7 of **1** and at C-2 and C-3 of **6**. Therefore, the HOMO of **4** corresponds to that of **1**. Note that the LUMOs of **1** and **6** interact with each other to give the LUMO of **4** because the orbitals at C-7 of **1** and at C-2 and C-3 of **6** are in phase with each other. Consequently, the loss of an electron from the HOMO of **3** reduces the antibonding character to give $\mathbf{3}^{\bullet+}$ with a bent structure like that of nonclassical $\mathbf{2}^{+}$,[1] while no such changes in the molecular geometry and electronic structure are expected for $\mathbf{4}^{\bullet+}$. In this sense, $\mathbf{4}^{\bullet+}$ may be termed a 'classical' radical cation, as a counterpart of the nonclassical radical cations, $\mathbf{2}^{\bullet+}$ and $\mathbf{3}^{\bullet+}$. The electronic coupling causes a rise in the HOMO level of **3** and a lowering of the LUMO level of **4** as compared with those of **1**, while the LUMO level of **3** and the HOMO level of **4** are not changed much. As described below, these changes are responsible for the observed red- and blueshifts of $\mathbf{3}^{\bullet+}$ and $\mathbf{4}^{\bullet+}$.

Analyses based on TD UB3LYP/cc-pVDZ calculations suggest that bands A, A′, and A″ and bands C, C′, and C″ of $\mathbf{1}^{\bullet+}$, $\mathbf{3}^{\bullet+}$ and $\mathbf{4}^{\bullet+}$ originate from the singly occupied MO (SOMO) → LUMO and the HOMO–X → LUMO ($X = 2$, 4, and 3 for $\mathbf{1}^{\bullet+}$, $\mathbf{3}^{\bullet+}$, and $\mathbf{4}^{\bullet+}$) transitions, respectively. Figure 4 is a schematic representation of the MOs associated with the calculated transitions for bands A, A′, and A″ and bands C, C′, and C″ of $\mathbf{1}^{\bullet+}$, $\mathbf{3}^{\bullet+}$, and $\mathbf{4}^{\bullet+}$, respectively. For convenience, pictures of the HOMO–X, SOMO, and LUMO of $\mathbf{1}^{\bullet+}$, $\mathbf{3}^{\bullet+}$, and $\mathbf{4}^{\bullet+}$ are replaced with the HOMO–(X + 1), HOMO, and LUMO of neutral **1**, **3**, and **4**, respectively, calculated using B3LYP/cc-pVDZ. Note that each HOMO–X is a similar type of MO with orbital coefficients only at the atoms of the benzhydrylidene subunits and that the distribution patterns of the orbital coefficients of the SOMOs and LUMOs are in line with those in Figure 3.

A key to explaining the observed red- and blueshifts for $\mathbf{3}^{\bullet+}$ and $\mathbf{4}^{\bullet+}$ as compared with $\mathbf{1}^{\bullet+}$ is the change in the energy levels of the MOs: those of the HOMO–4 of $\mathbf{3}^{\bullet+}$ and the HOMO–3 of $\mathbf{4}^{\bullet+}$ are very close to that of the HOMO–2 of $\mathbf{1}^{\bullet+}$. Furthermore, the energy levels of the SOMO of $\mathbf{3}^{\bullet+}$ and the LUMO of $\mathbf{4}^{\bullet+}$ rise and fall, respectively, while those of the LUMO of $\mathbf{3}^{\bullet+}$ and the SOMO of $\mathbf{4}^{\bullet+}$ are similar to those of $\mathbf{1}^{\bullet+}$. Namely, the red- and blueshifts of bands A′ and C′ for $\mathbf{3}^{\bullet+}$ are explained by the rise in the SOMO level and the unchanged LUMO and HOMO–4 levels, respectively, while the redshift and absence of a shift of bands A″ and C″ for $\mathbf{4}^{\bullet+}$ result from the unchanged SOMO and HOMO–3 levels and the lowering of the LUMO level, respectively. Note that the similar redshifts of bands A′ and A″ of $\mathbf{3}^{\bullet+}$ and $\mathbf{4}^{\bullet+}$ have different causes.

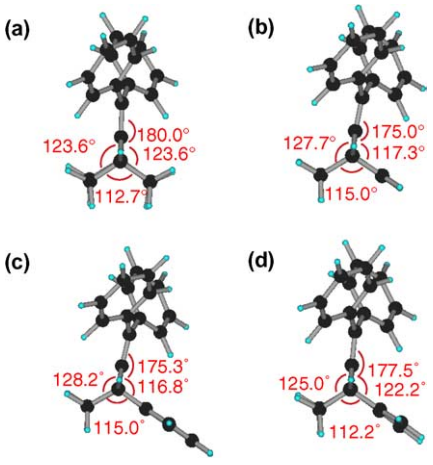

Figure 5. Side views of $\mathbf{1}^{\bullet+}$ (a), $\mathbf{2}^{\bullet+}$ (b), $\mathbf{3}^{\bullet+}$ (c), and $\mathbf{4}^{\bullet+}$ (d) optimized using UB3LYP/cc-pVDZ calculations.

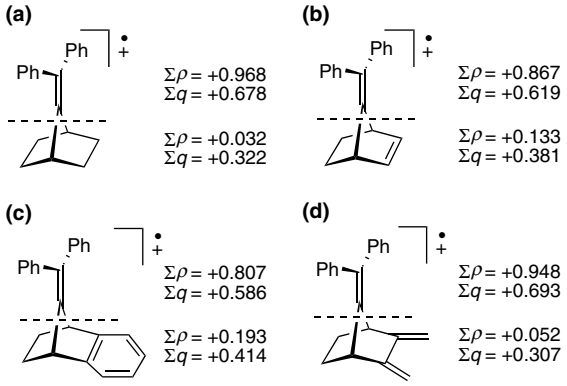

Figure 6. The sum of the partial spin (ρ) and charge (q) density of the benzhydrylidene subunit and residual subunit in $\mathbf{1}^{\bullet+}$ (a), $\mathbf{2}^{\bullet+}$ (b), $\mathbf{3}^{\bullet+}$ (c), and $\mathbf{4}^{\bullet+}$ (d) calculated using UB3LYP/cc-pVDZ.

The molecular geometry of $\mathbf{3}^{\bullet+}$ and $\mathbf{4}^{\bullet+}$ is summarized in Figure 5 together with that of $\mathbf{1}^{\bullet+}$ and $\mathbf{2}^{\bullet+}$.[1] The C-1–C-7–C-4 skeleton and the benzhydrylidene subunits of $\mathbf{3}^{\bullet+}$ bend to the side of the C-2–C-3 subunit by 5.7° [=(360.0° − 115.0°)/2 − 116.8°] and 4.7° (=180.0° − 175.3°), respectively, at the UB3LYP/cc-pVDZ level. Note that these angles are close to those (5.2° and 5.0°, respectively[1]) of $\mathbf{2}^{\bullet+}$. These findings support the nonclassical nature of $\mathbf{3}^{\bullet+}$ and are consistent with a suggestion from LFP spectroscopic studies. However, $\mathbf{4}^{\bullet+}$ has angles of 1.7° [=(360.0° − 112.2°)/2 − 122.2°] and 2.5° (=180.0° − 177.5°), respectively, corresponding to those (0.0° and 0.0°, respectively[1]) of $\mathbf{1}^{\bullet+}$ rather than those of $\mathbf{2}^{\bullet+}$. The differences in the angles between $\mathbf{3}^{\bullet+}$ and $\mathbf{4}^{\bullet+}$ are not large, but they are meaningful, taking into account the difference between the prototype $\mathbf{1}^{\bullet+}$ and nonclassical $\mathbf{2}^{\bullet+}$. These results lead us to regard $\mathbf{4}^{\bullet+}$ as a 'classical' radical cation without any significant electronic couplings between the C-7–C-8 and C-2–C-3 subunits in the SOMO, in contrast to $\mathbf{3}^{\bullet+}$. At the UB3LYP/cc-pVDZ level, a hypothetical dication $\mathbf{3}^{2+}$ bends more significantly, as does $\mathbf{2}^{2+}$,[1] while $\mathbf{4}^{2+}$keeps the nonbent structure,[15] supporting the efficient and negligible electronic coupling in the HOMOs of **3** and **4**, respectively (vide supra).

Next, we examined the electronic structure using the sum of the partial spin (ρ) and charge (q) density,[14] $\Sigma\rho$ and Σq, respectively, computed with DFT calculations, as shown in Figure 6. The values, $\Sigma\rho = +0.807$ and $\Sigma q = +0.586$, of the benzhydrylidene subunit in $\mathbf{3}^{\bullet+}$ decrease compared with those of $\mathbf{1}^{\bullet+}$, +0.968 and +0.678, respectively.[1] Accordingly, the values of the residual subunit (+0.193 and +0.414) increase compared with those of $\mathbf{1}^{\bullet+}$ (+0.032 and +0.322). The spin and charge distributions of $\mathbf{3}^{\bullet+}$ resemble those of $\mathbf{2}^{\bullet+}$ (+0.867 and +0.619 in the benzhydrylidene subunit, respectively,[1]) indicating the nonclassical nature of $\mathbf{3}^{\bullet+}$ whose spin and charge are delocalized not only to the benzhydrylidene subunit but also to the residual subunit. Conversely, the $\Sigma\rho$ and Σq values of the benzhydrylidene subunit in $\mathbf{4}^{\bullet+}$ (+0.948 and +0.693) resemble those of $\mathbf{1}^{\bullet+}$ (+0.968 and +0.678) but not those of $\mathbf{2}^{\bullet+}$, suggesting the 'classical' nature of $\mathbf{4}^{\bullet+}$ whose spin and charge are mainly localized on the benzhydrylidene subunit. These interpretations are consistent with the structure optimized with DFT calculation (Fig. 5).

In conclusion, we found the striking contrast in the molecular geometry and electronic structures of $\mathbf{3}^{\bullet+}$ and $\mathbf{4}^{\bullet+}$. TD DFT calculations successfully reproduced the UV/vis absorption spectra of $\mathbf{3}^{\bullet+}$ and $\mathbf{4}^{\bullet+}$ on LFP. DFT calculations also suggest bent and nonbent structures for $\mathbf{3}^{\bullet+}$ and $\mathbf{4}^{\bullet+}$, respectively. The contrast is attributed to the difference in the pattern of electronic coupling[16] (i.e., homoconjugation) between **3** and **4**. In particular, the topological agreement and disagreement of the orbitals at C-2, C-3, and C-7 of the HOMOs of **3** and **4** control the extent of the delocalization of spin and charge in $\mathbf{3}^{\bullet+}$ and $\mathbf{4}^{\bullet+}$. In this sense, the structure of π-electronic system at C-2 and C-3 is of importance for the appearance of the nonclassical and 'classical' nature of $\mathbf{3}^{\bullet+}$ and $\mathbf{4}^{\bullet+}$, respectively.

Acknowledgements

H.I. gratefully acknowledges financial support from a Grant-in-Aid for Scientific Research on Priority Areas (No. 417) from the Ministry of Education, Culture, Sports, Science, and Technology of Japan (No. 14050008). We also thank Professors M. Ueda (Tohoku University) and H. Niwa (UEC) for their generous considerations, and Dr. H. Ishii (UEC) and the late Mr. S. Shiina (UEC) for their efforts in preparing the samples.

Supplementary data

The DFT calculation results for **3**, $\mathbf{3}^{\bullet+}$, $\mathbf{3}^{2+}$, **4**, $\mathbf{4}^{\bullet+}$, and $\mathbf{4}^{2+}$, the absorption spectra of *n*-butyl chloride glassy matrices of **3** and **4** obtained after irradiation by γ-rays at 77 K, and the definition of the angles shown in Figure 5 (PDF). Supplementary data associated with this article can be found, in the online version, at doi:10.1016/j.tetlet.2005.08.167.

References and notes

1. Ikeda, H.; Namai, H.; Hirano, T. *Tetrahedron Lett.* **2005**, *46*, 3917–3921.
2. Hirano, Ohashi, and co-workers were the first to postulate the nonclassical nature of $\mathbf{2}^{\bullet+}$ on the basis of π-facial selective nucleophilic addition to $\mathbf{2}^{\bullet+}$ generated by PET reaction of **2**.[3]
3. Hirano, T.; Shiina, S.; Ohashi, M. *J. Chem. Soc., Chem. Commun.* **1992**, 1544–1546.
4. For recent studies of nonclassical cations, see Ref. 5 and the references cited therein.
5. Laube, T. *J. Am. Chem. Soc.* **2004**, *126*, 10904–10912.
6. (a) Weng, H.; Du, X.-M.; Roth, H. D. *J. Am. Chem. Soc.* **1995**, *117*, 135–140; (b) Roth, H. D.; Du, X.-M.; Weng, H.; Lakkaraju, P. S.; Abelt, C. J. *J. Am. Chem. Soc.* **1994**, *116*, 7744–7752.
7. PET reactions of **3** and **4** in the presence of nucleophile(s) were previously reported.[8]
8. Ishii, H.; Shiina, S.; Hirano, T.; Niwa, H.; Ohashi, M. *Tetrahedron Lett.* **1999**, *40*, 523–526.
9. Nanosecond time-resolved UV/vis absorption spectroscopy on LFP was carried out with a pulsed YAG laser (Continuum Surelite-10, Nd, THG, $\lambda_{ex} = 355$ nm, 55 mJ) using a Xe arc lamp (150 W) as the monitoring light.
10. The use of cationic sensitizers and chemically unreactive aromatic hydrocarbons, so-called cosensitizers, in acetonitirile is effective for observing radical cations in LFP experiments. Under cosensitized conditions, a substrate radical cation is formed via electron transfer from a cosensitizer to a photoexcited sensitizer followed by hole transfer from the cosensitizer radical cation to the substrate.
11. Similar absorption bands were observed in an *n*-butyl chloride glassy matrix of **3** and **4** irradiated with γ-rays at 77 K. See Supplementary data.
12. DFT and TD DFT calculations were performed using the program Gaussian 98.[13] Figures 4 and 5 were drawn using MolStudio software.[14]
13. *Gaussian 98* (*Revision A.11.4*), Frisch, M. J.; Trucks, G. W.; Schlegel, H. B.; Scuseria, G. E.; Robb, M. A.; Cheeseman, J. R.; Zakrzewski, V. G.; Montgomery, J. A.; Stratmann, R. E.; Burant, J. C.; Dapprich, S.; Millam, J. M.; Daniels, A. D.; Kudin, K. N.; Strain, M. C.; Farkas, O.; Tomasi, J.; Barone, V.; Cossi, M.; Cammi, R.; Mennucci, B.; Pomelli, C.; Adamo, C.; Clifford, S.; Ochterski, J.; Petersson, G. A.; Ayala, P. Y.; Cui, Q.; Morokuma, K.; Malick, D. K.; Rabuck, A. D.; Raghavachari, K.; Foresman, J. B.; Cioslowski, J.; Ortiz, J. V.; Stefanov, B. B.; Liu, G.; Liashenko, A.; Piskorz, P.; Komaromi, I.; Gomperts, R.; Martin, R. L.; Fox, D. J.; Keith, T.; Al-Laham, M. A.; Peng, C. Y.; Nanayakkara, A.; Gonzalez, C.; Challacombe, M.; Gill, P. M. W.; Johnson, B. G.; Chen, W.; Wong, M. W.; Andres, J. L.; Head-Gordon, M.; Replogle, E. S.; Pople, J. A. *Gaussian, Inc., Pittsburgh PA*, 1998.
14. For MolStudio (NEC), visit the web site at http://www.sw.nec.co.jp/APSOFT/SX/molstudio_e/index.html.
15. For the detail of the calculations for $\mathbf{3}^{2+}$ and $\mathbf{4}^{2+}$, see Supplementary data.
16. For suggestions of similar electronic coupling through space and bond in reactive radical cations, see Refs. 17.
17. (a) Ikeda, H.; Hoshi, Y.; Kikuchi, Y.; Tanaka, F.; Miyashi, T. *Org. Lett.* **2004**, *6*, 1029–1032; (b) Ikeda, H.; Hoshi, Y.; Miyashi, T. *Tetrahedron Lett.* **2001**, *42*, 8485–8488; (c) Ikeda, H.; Takasaki, T.; Takahashi, Y.; Konno, A.; Matsumoto, M.; Hoshi, Y.; Aoki, T.; Suzuki, T.; Goodman, J. L.; Miyashi, T. *J. Org. Chem.* **1999**, *64*, 1640–1649; (d) Ikeda, H.; Minegishi, T.; Abe, H.; Konno, A.; Goodman, J. L.; Miyashi, T. *J. Am. Chem. Soc.* **1998**, *120*, 87–95; (e) Brede, O.; David, F.; Steenken, S. *J. Chem. Soc., Perkin Trans. 2* **1995**, 23–32; (f) Williams, F. *J. Chem. Soc., Faraday Trans.* **1994**, *90*, 1681–1687; (g) Tamai, T.; Mizuno, K.; Hashida, I.; Otsuji, Y. *J. Org. Chem.* **1992**, *57*, 5338–5342; (h) Tojo, S.; Toki, S.; Takamuku, S. *J. Org. Chem.* **1991**, *56*, 6240–6243; (i) Pac, C. *Pure Appl. Chem.* **1986**, *58*, 1249–1256.